

MANUSCRIPT

Characteristics of the ambient seismic field on a large-N seismic array in the Vienna basin

Authors:

Sven SCHIPPKUS
University of Vienna
Department of Meteorology and Geophysics,
Althanstraße 14,
1090 Vienna, Austria
Corresponding Author: sven.schippkus@univie.ac.at

Mikaël GARDEN
OMV E&P GmbH,
Geophysics Department,
Trabrennstraße 6-8,
1020 Vienna, Austria

Götz BOKELMANN
University of Vienna
Department of Meteorology and Geophysics,
Althanstraße 14,
1090 Vienna, Austria

Characteristics of the ambient seismic field on a large-N seismic array in the Vienna basin

Sven Schippkus¹, Mikaël Garden² and Götz Bokelmann¹

¹Department of Meteorology and Geophysics, University of Vienna, Vienna, Austria,

Corresponding Author: sven.schippkus@univie.ac.at

²OMV E&P GmbH, Geophysics Department, Vienna, Austria

March 9, 2020

Abstract

The ambient seismic field is now routinely used for imaging and monitoring purposes. Most commonly, applications aim at resolving crustal-scale features, and utilize ocean-generated surface waves. At smaller scales and at frequencies above the microseismic peaks, local sources of seismic energy, often anthropogenic, are dominant and understanding of their contributions to the ambient seismic field becomes important in order to apply ambient noise techniques. This study uses data of an industrial-scale seismic deployment covering $\sim 500\text{km}^2$ with 10,532 stations, each equipped with several co-located 10Hz geophones, to provide unique insight into anthropogenic sources of seismic energy in a suburban to rural area. We compute amplitude levels, their distance-dependency, power spectral densities, and spectrograms to describe the source characteristics. The sources we observe in great detail include windmills, a railway track and trains, cars, oil pumpjacks, power lines, gas pipelines, and airplanes. These sources exhibit time-dependent behaviour that is illustrated strikingly by videos of amplitude levels in certain frequency bands that we provide as electronic supplement. The data described in this study are a potential resource for future studies, such as automatic signal classification, as well as underground imaging using microseismic noise or the sources presented here.

Keywords— Ambient Seismic Field, Seismic Sources, Dense Array

18 Introduction

19 Dense arrays of hundreds to thousands of seismic stations are common in industrial applications,
20 mostly for exploration of fossil resources. Recently, these arrays have become subject of scientific
21 research, as they allow unique insights that are usually unattainable through scientific funding
22 opportunities. The maturing of ambient noise techniques allows these techniques to become a
23 routine part of seismologists' toolkit (Nakata et al., 2019, and references therein); applying them at
24 local scale is a next natural step (e.g., Nakata et al., 2015; de Ridder & Biondi, 2015; Mordret et al.,
25 2013, 2018; Meng & Ben-Zion, 2018; Spica et al., 2018; Brenguier et al., 2020; Mordret et al.,
26 2020). In recent years, it has become increasingly clear that the description and analysis of seismic
27 sources that generate the ambient seismic field are essential aspects to advance the field in the future
28 (e.g., Karplus & Schmandt, 2018, and references therein).

29 At frequencies below 1Hz, ocean-driven mechanisms have been identified and described that
30 continuously induce seismic noise that is measured all around the globe (Longuet-Higgins, 1950;
31 Hasselmann, 1963; Ardhuin et al., 2011). Ardhuin et al. (2011) classify these mechanisms into
32 primary (wave-to-land interaction) and secondary (wave-to-wave interaction), providing explanations
33 for the primary ($T \sim 14\text{s}$) and secondary ($T \sim 7\text{s}$) microseismic peaks, as well as the Earth's hum at
34 periods $T > 30\text{s}$. In central Europe, the dominant sources are located in the North Atlantic (Juretzek
35 & Hadzioannou, 2016, 2017). These lower microseismic frequencies are now routinely used for
36 imaging (e.g., Lin et al., 2008; Roux, 2009; Ren et al., 2013; Lu et al., 2018; Kästle et al., 2018;
37 Schippkus et al., 2018) and monitoring (e.g., Brenguier et al., 2008, 2014; Lecocq et al., 2017) of
38 the subsurface.

39 At frequencies above 1Hz, dominant seismic sources are generally of anthropogenic nature.
40 Traffic and machinery in particular have been shown to induce strong signals that may dominate the

41 seismic recordings at certain frequencies, and efforts have been made to discriminate and understand
42 the contributors to the ambient seismic field at these frequencies (e.g., Nakata et al., 2015; Riahi &
43 Gerstoft, 2015; Stammel & Ceranna, 2016; Fuchs et al., 2017; Meng & Ben-Zion, 2018; Brenguier
44 et al., 2019). These sources are usually thought to degrade station performance of permanent
45 networks, e.g., when new windmills are installed near a long-operating seismic array (Stammel
46 & Ceranna, 2016). Riahi & Gerstoft (2015) used data of the Long Beach seismic array (5,200
47 geophones) to describe traffic-generated seismic noise, including Metro trains, cars, and airplanes, in
48 an urban region. Brenguier et al. (2019) were able to utilize such anthropogenic sources, in their case
49 trains, for seismic monitoring of the San Jacinto Fault Zone. It is clear that a good understanding of
50 the ambient seismic field is essential for this kind of application.

51 This study aims at giving insight into the complexities of the ambient seismic field in a
52 suburban to rural area with windmills, train traffic, oil pumpjacks, and other sources of seismic
53 energy. For this, we use data of a dense seismic array (10,532 stations) that was deployed for one
54 week in the eastern Vienna basin, near Gänserndorf, to discriminate, characterize, and describe the
55 properties of these anthropogenic sources. This study is further intended as a reference for future
56 studies, such as ambient noise tomography at shallow depths. The data may also become a potential
57 benchmark dataset for new and established signal-classification algorithms, a field that is advancing
58 rapidly in recent years due to the advent of machine learning techniques (e.g., Kong et al., 2018;
59 Chamarczuk et al., 2019).

60 **Experiment Setup and Data**

61 The study area is located just west of the Austria-Slovakia border in the Vienna basin around the city
62 of Gänserndorf (Fig. 1). The stations partially cover the Matzen oil field in the northwest, which

63 has been in production since 1949 with 12,300 barrels of oil per day and a total proven reserve of
64 510 million barrels (Brix & Schultz, 1993). The main purpose of the seismic survey was active
65 seismic exploration (Garden & Zühsdorff, 2019).

66 The 10,532 seismic stations were set up with 40m in-line and 400m cross-line spacing,
67 with a NNE/SSW in-line orientation, and minor deviations from the planned lines (Fig. 1). Each
68 seismic station is equipped with 12 or 24 densely co-located (within 1m²) 10Hz-geophones (Sercel
69 JF-20DX). In total, ~150,000 geophones were deployed for this survey. The data at each station is
70 stacked before being recorded by autonomous nodal digitisers (AutoSeis HDR) at 500Hz sampling
71 rate. Prior to the start of active measurements, the stations recorded the ambient seismic field, i.e.,
72 the data used in this study. The data was recorded over the course of six days from January 18th
73 2018 to January 23rd 2018 during daytime only, from 06:30 to 22:00 local time (UTC+1). That way,
74 the stations recorded up to 92.5 hours of data. The stations in the southeast of the study area were
75 deployed during the measurement and have data available for as little as 12 minutes (Fig. 1).

76 The array has a number of faulty stations that did not record usable data. Those stations
77 were dominated by artifacts and glitches; we do not use the data from those stations further. We
78 identify those stations by extremely high power spectral densities (higher than 1E12 c² m²/s² Hz) at
79 frequencies between 0.1 and 1Hz. 816 (7.7%) stations are classified as faulty. Thanks to the size of
80 the array with 10,532 total stations, excluding 816 stations that are randomly distributed throughout
81 the array has negligible impact on our analysis. The fact that 12 or 24 geophones are co-located and
82 stacked increases signal-to-noise ratio significantly, because self-noise of the sensors is mitigated,
83 but may also make stations potentially unusable if only one of those geophones is faulty.

84 We removed the instrument response of the geophones from the data, but a scaling factor
85 for the (unknown) transfer function of the AutoSeis HDR digitisers remains. Thus, amplitudes are
86 given in c times meters per second, where c represents the conversion from counts (output of the

87 digitiser) to Volts (output of the geophone), and not directly in physical units of ground motion.

88 The study area includes a remarkable breadth of potential sources of seismic signals that
89 allow unique insight into their properties. The area encompasses cities and towns, the main railway
90 track that connects Vienna to the Czech Republic, dozens of windmills, hundreds of oil pumpjacks,
91 power lines, the Baumgarten gas hub (Schneider et al., 2018) and underground gas pipelines, car
92 and truck traffic on roads (see Fig. 2), as well as airplane traffic of the nearby Vienna International
93 Airport. We do not treat cities and towns as individual potential noise sources, because they are
94 ultimately an amalgamation of various sources such as traffic, people, and machinery. Separating
95 their individual contributions at this close distance is not straightforward, and exceeds the scope of
96 this paper.

97 **Results**

98 To gain insight into the properties of each of the noise sources recorded on the array, we perform
99 five analyses: mean absolute amplitudes recorded at each station as a function of time provide
100 insight into the spatial and temporal distribution of sources, including moving sources such as trains.
101 Power-spectral densities (PSDs) of stations that are located close to noise sources reveal the spectral
102 characteristics of the sources, especially stationary ones like windmills and oil pumpjacks. PSD
103 amplitudes versus distance allow to study the distance-dependent impact of those noise sources at
104 certain frequencies and propagation regimes. Spectrograms of particularly-well recorded events
105 and continuous sources provide further detailed insight into their characteristics. Beamforming at
106 frequencies near the secondary microseismic peak illustrates the capability of the 10Hz-geophones
107 to reliably record such frequencies, and their potential for classical ambient noise applications.

108 We computed mean absolute amplitudes for all stations in 1-minute time-windows for the

109 available time frame for unfiltered, and filtered (in three frequency bands: 0.5-2Hz, 2-8Hz, 8-20Hz)
110 data. Maps of the amplitude levels averaged over the entire duration of deployment (Fig. 2a-c)
111 reveal a spatially consistent distribution of amplitude levels that can be attributed to noise sources in
112 the study area (Fig. 2d). Locations of sources are extracted and compiled from OpenStreetMap
113 contributors (2017), Interessengemeinschaft Windkraft Österreich (2020), and Gas Connect Austria
114 GmbH (2020), and OMV E&P GmbH (pers. comm.).

115 At 0.5-2Hz, we observe a generally even distribution of amplitudes. Stations record slightly
116 increased amplitude levels in the northwest, near the wind farm Prottendorf-Ollersdorf (PO; red triangles
117 in Fig. 2d). At 2-8Hz, we additionally observe increased amplitudes near the railway track, oil
118 pumpjacks, and the Baumgarten gas hub. At 8-20Hz, roads and power lines emerge as visible noise
119 sources, in addition to the sources visible at lower frequencies.

120 Videos of the mean absolute amplitudes with 1-minute time-resolution provide a unique and
121 remarkably clear illustration of daily activity in the study area (Text S1, and Videos S1-S4). We
122 observe increased noise levels and more moving sources, such as cars and trains, during weekdays,
123 and less activity on the weekend. The wind farm PO emerges as a dominant noise source with
124 time-variable activity. In contrast, the other windmills in the study area (blue triangles in Fig. 2d)
125 appear to generate significantly less seismic signal (Videos S1-S4). Oil pumpjacks in the region
126 (purple inverted triangles in Fig. 2d) induce increased amplitude levels at frequencies above 2 Hz,
127 and are one of the dominant sources at these frequencies (Videos S3, S4). The spatial distribution of
128 high amplitude levels in the northwest matches particularly well with the locations of the wind farm
129 PO and oil pumpjacks (Fig. 2, Videos S3-S4). In addition to anthropogenic sources, the videos also
130 visualize weather-related events (Text S1, Fig. S3, and Video S2).

131 Binned and stacked PSDs for stations near potential noise sources (i.e., within 200m distance)
132 exhibit distinct spectral features that can be attributed to the respective noise sources (Fig. 3).

133 Stations near windmills (Fig. 3a, b) show clear spectral peaks and increased amplitudes at frequencies
134 from 1 to 10 Hz, stations near the railway track (Fig. 3c), and roads (Fig. 3e) have smoother spectra
135 ("less peaky") and increased amplitudes at frequencies above 10Hz. Stations near power lines (Fig.
136 3f) and gas pipelines (Fig. 3g) show two distinct trends between 2 and 10 Hz. Stations that are
137 not near any of the identified noise sources (i.e., in at least 1000m distance), show clearly lower
138 amplitudes across all frequencies above 1Hz.

139 To ensure that there is no significant cross-contamination between the different sources and
140 their impact on the PSDs for the following interpretation, we additionally limit the set of stations
141 attributed to a single source to stations that are not within 400m of any other noise sources (Fig. S2).
142 This selection further focuses the PSD distributions, especially those of stations near oil pumpjacks,
143 power lines, and gas pipelines, as they are often located in close proximity to other sources (e.g.,
144 oil pumpjacks near roads) or are relatively weak. This selection also implicitly excludes cities
145 and town centers, as there are multiple sources nearby in more densely populated areas. However,
146 this selection does eliminate a considerable amount of stations for further analyses and in the case
147 of stations near windmills that are not part of the wind farm PO, all of them (Fig. S2b). Still,
148 these stations show particularly distinguishable spectral features not seen on other stations even
149 when including other nearby sources (Fig. 3). The exclusion of stations near other sources can be
150 detrimental for stations near strong persistent sources, such as windmills, but appears to be useful for
151 stations near weak and broadly distributed sources, such as power lines. Therefore, both approaches
152 (exclusion vs. no exclusion) provide important insight and are useful for discussion.

153 Regardless of this selection, stations appear to reliably recover signals as low as 0.2 Hz. There
154 are a number of low-amplitude peaks from 0.2 to 1 Hz observed across essentially all stations with
155 similar amplitudes. Above 1Hz, spectral signatures of each source start to dominate the spectra of
156 stations near those sources.

157 PSD amplitudes as a function of distance at certain frequencies reveal distinctly different
158 patterns for different noise sources (Fig. 4). Here, we exclude stations within 400m to any other
159 source to reduce some of the cross-contamination between different sources, while still allowing
160 us to fit the data reliably. Wherever we do observe a distance-dependent decay of amplitudes they
161 appear to follow a power law description (black lines in Fig. 4). At 0.48 Hz, no source appears to
162 induce a significant distance-dependent decay. Windmills of PO have significant impact on stations
163 in up to a few hundred meters distance at 1.13 Hz (Fig. 4). At 10 Hz, we observe significant impact
164 of windmills of PO and the railway track on stations up to one kilometer distance. Other sources,
165 such as oil pumpjacks and roads, induce increased amplitude in up to a few hundred meters distance.
166 Power lines appear to generate seismically recorded signal up to tens of meters away. At 50 Hz, the
167 frequency of the power grid, power lines become one of the most significant sources for stations up
168 to 100 m away. The signal recorded near other sources (windmills of PO, railway, oil pumpjacks,
169 and roads) also decays rapidly down to background noise levels over tens to a few hundreds of
170 meters (Fig. 4). It is clear that the distance up to which sources are relevant depends on the seismic
171 energy emitted by the source, the propagation regime, and the level of background noise.

172 Representative spectrograms of 10-minute windows provide further insight into the spectral
173 and temporal properties of the different noise sources (Fig. 5). We show spectrograms for the wind
174 farm PO (Fig. 5a), a different windmill (Fig. 5b), trains (Figs. 5c, 6a), an oil pumpjack (Figs. 5d,
175 6b), cars (Figs. 5e), a power line (Fig. 5f), a gas pipeline (Fig. 5g), no nearby source (Fig. 5h), and
176 an airplane (Fig. 5i). Some sources excite energy continuously over time scales of tens of minutes
177 to hours and even days, such as wind mills, oil pumpjacks, power lines and potentially gas pipelines.
178 Other sources are distinct events, such as passing trains, cars, and airplanes.

179 We perform beamforming at frequencies near the secondary microseismic peak at 0.2-0.5 Hz
180 (Suppl. text S2, Fig. S1). At these frequencies, there appears to be no major source inside the array

181 or very close-by and the plane-wave assumption of classical beamforming is likely reasonable. We
182 find that the array records seismic energy arriving from northwest (301 degrees, 3.4 km/s), consistent
183 with ocean-generated Rayleigh waves in the North Atlantic (Juretzek & Hadzioannou, 2016, 2017).
184 At higher frequencies this assumption does not hold any longer, and we do not compute beam powers
185 for them. At lower frequencies we do not retrieve coherent signals and the beamforming results
186 become unreliable.

187 Discussion

188 We are able to clearly distinguish the seismic characteristics of several anthropogenic sources in the
189 study area (Figs. 2, 3, 4, 5, 6). However, our analysis and following discussion are based on the
190 assumptions that (i) we have identified and mapped all relevant sources of seismic signal in the area,
191 (ii) sources of a given type have similar characteristics, (iii) site effects are not important, and (iv)
192 that we have sufficiently eliminated cross-contamination of nearby sources where necessary. In the
193 following, we first discuss each of those assumptions before discussing each source in greater detail.

194 The locations of seismic sources are extracted and compiled from several sources, and some
195 may be prone to errors. Locations of windmills (Interessengemeinschaft Windkraft Österreich, 2020)
196 are precise, and additional information about the windmill model is available. Infrastructure data,
197 such as roads, railway tracks, power lines are extracted directly from data provided by OpenStreetMap
198 contributors (2017). While this data is crowdsourced and relies on the general public for accuracy, it
199 is generally considered to be precise and rich in detail. The locations of gas pipelines we use in this
200 study are based on the online map provided by Gas Connect Austria GmbH (2020). We may have
201 introduced location errors up to tens of meters during the extraction of this information, as this was
202 done visually. Oil pumpjack locations are precise, but include all locations in the area. There is no

203 distinction between active and inactive pumpjacks. We believe these sources to be the entirety of
204 relevant seismic sources in the region, and our analysis has not given any indication that we may
205 have neglected other major sources.

206 We assume that all individual sources of a given type behave similarly, which for some
207 sources is clearly invalid. The distribution of power spectral densities for power lines and gas
208 pipelines show two to three distinctly emerging maxima between 2 and 10 Hz (Fig. 3f, g). Similarly,
209 amplitudes at 50 Hz for stations near power lines (Fig. 4) show that some stations do not follow a
210 power law decay of amplitudes with distance, and instead are at background levels of noise even
211 close to the power lines. Distinct source events, such as trains and cars, are obviously also dependent
212 on the individual source itself (e.g., freight train vs passenger train, or different cars, see Fig. 5,
213 and electronic supplement). These considerations are indeed what lead to the distinction between
214 the windmills of the wind farm PO and other windmills, as these expose different characteristics
215 across every measure we analyse in this study (Figs. 2, 3, 4, 5). Therefore, caution is advised when
216 interpreting our findings, in particular patterns that may be explained simply by different models of
217 the same source type.

218 We further neglect the potential impact of site effects on recorded amplitudes. At large scale,
219 the entire study region is covered with Quaternary sediments, and there are no hard rock sites. At
220 smaller scale, very local effects such as poor coupling of sensors, and soil properties may impact
221 station performance and thus recorded amplitudes. We do in fact find that a number of stations show
222 very high amplitudes compared to others (Figs. 3, 4), and these do not appear to correlate with any
223 known noise source. However, they also do not form a spatially coherent picture and appear to be
224 distributed randomly throughout the array. Therefore, these stations are likely not indicative of
225 geophysical site effects, and are more likely to have poor coupling or data quality issues. These
226 stations should therefore not be considered in the following interpretation and discussion, and a

227 stricter or more elaborate selection of stations may enhance some insights.

228 To eliminate cross-contamination between different sources, we put constraints on the stations
229 included for analysis of a given source by distance to any other source. We chose a 400m distance
230 threshold as a compromise to balance that sources are often located close-by to other sources and
231 that only few sources show significant impact at greater distances, namely windmills of PO and the
232 railway track at 10Hz (Fig. 4). A stricter threshold would exclude a very large number of stations
233 from our analyses, and thus reduces our ability to observe consistent trends, while not providing
234 new insights.

235 Therefore, we believe our analysis allows to make reliable observations that relate to the
236 individual anthropogenic seismic sources. In the following, we discuss each of the potential sources,
237 in a sequence of decreasing impact on the ambient seismic field in the study area.

238 Windmills

239 As described above, we differentiate two sets of stations near windmills: those near the wind farm
240 Prottes-Ollersdorf (PO, red triangles in Fig. 2d) with 13 windmills and those near other windmills
241 (blue triangles in Fig. 2d). Stations near PO have generally higher amplitudes than all other stations
242 (Figs. 2, 3, 5), and show different spectral peaks than those near the other windmills (Figs. 3a, b, 5a,
243 b). The prominent spectral peak at 1.13Hz, recorded on all stations, appears to be induced by the
244 windmills of PO, as the peak's amplitude is highest near the windmills (Fig. 3). Likewise, there is a
245 clear amplitude decay with distance for stations near PO at 1.13 Hz and 10Hz (Fig. 4). However,
246 amplitudes decay down to background-noise levels after about 500m. We find that at 1.13Hz, only
247 the windmills of PO show a significant distance-dependent decay of measured amplitudes. The
248 other windmills have only few nearby stations that are not excluded due to the vicinity to other
249 sources (Fig. 4), and we do not observe a conclusive distance-dependent trend at any of the chosen

250 frequencies.

251 The spectrogram reveals that the windmills of PO often operate at varying frequency (Fig. 5a).
252 Wherever the amplitude is decreased, the dominant spectral peaks shift to lower frequencies. This
253 effect has also been observed by Hu *et al.* (2019). The other windmills induce less seismic energy
254 and appear to operate at constant frequency. The windmills of PO (Enercon E-101) produce 3.05
255 Megawatts each with a maximum rotation speed of 0.24 rps (revolutions per second) and 50m long
256 blades, while the other windmills (Enercon E-70/E4) produce 1.8 Megawatts each with maximum
257 0.36 rps and 35m long blades (Interessengemeinschaft Windkraft Österreich, 2020). Furthermore,
258 Enercon E-101 windmills can start operation at lower wind speeds than E-70/4 (2.0m/s vs 2.5m/s).
259 It is therefore not surprising that the windmills of PO induce more seismic energy due to operation
260 at lower wind speeds, longer blades, and higher energy output. Similarly, it is not surprising that
261 they induce different spectral peaks (Fig. 5a, b). The 0.48Hz peak visible across all stations (Fig. 3)
262 may possibly be attributed to the first overtone of the maximum rotation speed of Enercon E-101
263 windmills (0.24Hz), but we do not find a conclusive distance-dependent amplitude decay at this
264 frequency (Fig. 4). It is possible that this spectral peak does not decay strongly at this frequency,
265 because the wavelength of a Rayleigh wave at 0.48Hz (\sim 5km) is only slightly smaller than the
266 aperture of the array. Also note that the spectral peak at 1.13 Hz is not an overtone of 0.24Hz.

267 Windmills as sources of seismic signal and their impact on the performance of permanent
268 seismic stations have recently become an issue for network operators. Stammler & Ceranna
269 (2016) showed that the seismic energy induced by windmills correlates well with wind-speed and
270 contains distinct spectral peaks that overpower the background noise at frequencies of 1-7Hz. Our
271 observations corroborate this with clear spectral peaks in this frequency range, and beyond (Fig. 3a,
272 b).

273 Stammler & Ceranna (2016) were further able to identify a power law decay of amplitudes

with distance from about 1km up to 8km distance, the distance of the Gräfenberg array to the newly installed windmills. Our data set allows insight into the distance-dependent decay from a few meters up to a few kilometers distance, complementing their insight. Note that our analysis is based on 10Hz-geophones deployed in a suburban to rural region, and in a sedimentary basin. Therefore, high amplitude levels are expected throughout the entire array, which may hinder our ability to estimate amplitude decay precisely. Gortsas *et al.* (2017) modelled the generation of seismic and infrasound noise by windmills numerically. In their model, displacement amplitudes decay with distance from the windmill r by the power law $r^{-0.9}$, similar to surface-wave decay (r^{-1}). This is in contrast to the decay of PSD values reported by Stammler & Ceranna (2016) that follow $r^{-2.7}$, exceeding body-wave decay (r^{-2}). We find two different power law decay exponents at 1.13Hz with $r^{-0.8}$ and at 10Hz with $r^{-2.6}$, potentially representing both propagation regimes. However, the background noise level is reached after \sim 250m at 1.13Hz, and after \sim 750m at 10Hz. This may bias our estimate of the power law decay of windmill-generated seismic energy at 1.13Hz to be slower than it is in reality. Hu *et al.* (2019) report PSD amplitude decay exponents from -0.52 to -1.87, depending on frequency, and they similarly suggest that this may be related to body-wave (near-field) and surface-wave (far-field) propagation regimes. Their results are based on four stations only though. Edwards (2015) finds surface-wave propagation on four stations at 2.41Hz to 4.83Hz, corresponding to the turbine blade-pass harmonics of the windmill they investigated. It may appear, and our data also suggests, that different propagation regimes are active at different frequencies. We observe cylindrical decay at 1.13 Hz (likely surface waves), and spherical decay at 10 Hz (potentially seismo-acoustic propagation). The fact that Stammler & Ceranna (2016) observe spherical decay at 1-8 km distance, however, raises questions about a seismo-acoustic mechanism at such long distances, but their results are based on few stations only. In any case, geometrical effects on amplitude-decay exceeds the impact of frequency-dependent attenuation considerably and is the

298 likely explanation for the observed trends.

299 **Trains**

300 Trains are moving sources that can be easily identified in the videos of amplitude levels over time
301 (Text S1, Videos S1-S4). The railway track is the strongest source above 10Hz (Fig. 3c), and it
302 induces no significant narrowband spectral peaks, different from stations near windmills (Fig. 3a,
303 b). The spectrogram, however, shows clear evidence for a strong influence of the traction current
304 (operated at 16.7Hz) on the seismic recordings (Fig. 5c). The continuous horizontal lines present
305 throughout the 10-minute spectrogram are the first and even overtones of the traction current (1st,
306 2nd, 4th, 6th, ... overtone). Odd overtones after the first are either extremely weak or not excited
307 (Fig. 5c).

308 Fuchs et al. (2017) have described the spectral features of passenger and freight trains on the
309 same railway track that crosses our study area. They observed equidistant spectral lines and argued
310 that they are likely induced by the interaction of the trains' axles with the railway track as quasi-static
311 sources. Brenguier et al. (2019) modelled this interaction and confirmed the quasi-static loading
312 mechanism. The temporary broadband station used by Fuchs et al. (2017) is part of the AlpArray
313 project (Hetényi et al., 2018) and located ~2km to the west of our array. It is not surprising that
314 we observe the same spectral features they described. Unlike Fuchs et al. (2017), however, we do
315 observe a clear Doppler effect for most passing trains. In Figure 6a, we identify a frequency shift of
316 ~3 Hz after the train passes the seismic station. Fuchs et al. (2017) were limited to a single station
317 in 1.4km distance to the track, whereas in our study we have several stations in distances of tens of
318 meters to the track. Therefore, we are able to observe a clear Doppler effect that is not mitigated by
319 distance to the moving source.

320 Brenguier et al. (2019) demonstrated the capability of train signals being used as a source for
321 seismic monitoring. They correlated train-generated seismic signals to reconstruct body waves that
322 propagate through the San Jacinto Fault Zone and are thus sensitive to its structure. This can in
323 principle be applied to monitoring of other subsurface features that change seismic properties over
324 time as well, such as the Matzen oil and gas field in our study area.

325 **Oil pumpjacks**

326 Oil pumpjacks continuously generate strong and characteristic seismic signals. In addition to
327 windmills and the railway track, those pumpjacks represent the third major seismic source at 2-20Hz
328 (Fig. 2b, c). The spatial distribution of increased amplitudes in the northeast at those frequencies is
329 particularly well-explained by the presence of oil pumpjacks (Fig. 2d).

330 Amplitudes peak around 10-20 Hz in the PSDs, with some minor peaks at 1-10 Hz (Fig.
331 3d). These are likely related to the machinery, and the up-and-down motion of those pumpjacks.
332 There are no distinct peaks that can be clearly attributed to the pumpjacks at frequencies below 1 Hz,
333 which one may expect due to their movement. In fact, we do directly observe the periodical motion
334 of an oil pumpjack in the seismic trace and spectrogram of a nearby station (Figs. 5d, 6b), with a
335 repeating period of \sim 16s. The highest amplitude for this station is found at \sim 40 Hz, but this peak
336 in the spectrogram is not represented well in the distribution of PSDs (Figs. 3d, S2d). This is an
337 indication that our oil pumpjack locations are potentially heavily biased towards inactive locations,
338 and that stations near inactive oil-pumpjacks may thus dominate the PSDs. Additionally, not all
339 locations that are still equipped with oil pumpjacks may be active at all times.

340 Stations near oil pumpjacks mostly show low amplitude-decay rates ($r^{-0.1}$ to $r^{-0.6}$), and the
341 power laws at 0.48Hz and 1.13Hz do not appear to describe the actual observed amplitudes well
342 (Fig. 4). Instead, the power law fit appears to be heavily biased by a number of stations near the

343 oil pumpjacks (at 50-250m distance) that show increased amplitude levels apparently unrelated
344 to the pumpjacks. At 10Hz, however, the amplitude decay is quite clear and is more resembling
345 surface-wave propagation ($r^{-0.6}$, Fig. 4). A few stations show low amplitudes quite close to
346 pumpjacks.

347 Cars

348 Stations near the roads show passing cars and trucks that induce seismic signals at frequencies of \sim 2
349 Hz and above (Figs. 3, S2). PSD amplitudes at these frequencies are amongst the highest across all
350 sources, surpassed only by stations near the railway track, and with a considerable spread.

351 Car traffic is not equally distributed among all kinds of roads. For our analysis, we selected all
352 roads except minor roads that are only used very infrequently and mainly for agricultural machinery.
353 There is no highway in the study area. Still, the PSDs show a spread of several orders of magnitude
354 in amplitude for the selected stations, in particular at 10 - 100 Hz (Figs. 3, S2). Simply speaking, a
355 few roads show very high traffic, mostly near Gänserndorf in the west, while others see very little
356 traffic (see suppl. text S1, and electronic supplement).

357 Depending on the type of road, and the traffic density on it, cars could also be utilized as
358 continuous seismic sources. In contrast to train traffic, however, it seems that we do not observe a
359 quasi-static loading mechanism, as there are no equidistant spectral lines visible in the spectrograms
360 (Figs. 5e). Additionally, cars do not follow a strict schedule that would constitute a reliably-repeating
361 source to use for monitoring purposes over time (Brenguier et al., 2019). Still, on high-traffic roads,
362 such as highways, the roads themselves can potentially be seen as a continuously excited noise
363 source; it seems impossible with the current array spacing to distinguish individual cars and their
364 seismic impact during times of high traffic (Riahi & Gerstoft, 2015).

365 **Power Lines**

366 The power grid, operating at 50Hz in Austria, generates strong spectral lines at 50Hz and its second
367 overtone (150Hz) on nearby stations (Fig. 5f). This is similar to the observation of the railway
368 traction current, where we also observe even overtones of the base frequency (Figs. 5c, 6a). It
369 appears certainly possible that the power grid couples electro-magnetically into the seismometers
370 over distances of tens of meters due to very high voltages.

371 This does, however, not explain that stations near power lines also exhibit increased amplitudes
372 at frequencies lower than 50Hz (Figs. 2c, 5f). These stations are located mostly in fields, such as the
373 ones at around 48.33°N, 16.8°E, where there is no other seismic source nearby. The amplitude video
374 for 8-20Hz (Text S1, Video S4) reveals that increased amplitude levels for stations near power lines
375 are highly time-dependent. The episodes of increased amplitudes, usually over tens of minutes, are
376 spatially coherent. That is, if nearby power lines induce increased amplitudes on seismometers, they
377 do so along a section that is at least a few kilometers long. The spectrogram (Fig. 5f) shows such an
378 example of increasing amplitudes over minutes, with a few continuous spectral peaks and the onset
379 of an additional spectral peak (all between 10 and 50Hz). In contrast to windmills, amplitude levels
380 do not appear to coincide with changes in dominant frequencies.

381 People sometimes report hearing a hissing or crackling sound near power lines, an effect
382 known as corona discharge that can cause audible noise as it ionizes the air around the power
383 line (Loeb, 1965). This effect is certainly relevant at higher, audible frequencies, but may also
384 induce infrasound ($f < 20\text{Hz}$) that could couple seismo-acoustically into the ground and seismometers
385 (e.g., Evers *et al.*, 2007; Schneider *et al.*, 2018). Another possible mechanism is mechanical
386 interaction of the transmission towers (spaced at $\sim 300\text{m}$ in the study area) with the ground, and
387 propagation of seismic surface waves from the tower to the seismometers. Transmission towers

388 are certainly vibrating due to interaction with wind. However, any naturally-induced mechanism
389 is unlikely to explain continuous spectral lines with constant frequency (Fig. 5f). Indeed, wind
390 speed and precipitation data from a meteorological station in the array reveal that there appears to
391 be no connection between increased seismic amplitudes near power lines at 8-20Hz and increased
392 wind speed (see suppl. text S1, and electronic supplement). Instead, these observations point to
393 seismo-acoustic coupling of corona discharge, where higher electric energy transfer along a section
394 of the power grid could induce more acoustic sound and thus increased seismic amplitudes.

395 At 50Hz, amplitudes decay with $r^{-1.1}$ when considering stations near power lines that are
396 in at least 400m distance from any other source (Fig. 4). However, when excluding those stations
397 that do not exhibit increased amplitudes near power lines, amplitudes decay with $r^{-2.5}$ (grey line in
398 Fig. 4). This points to spherical propagation, suggesting that seismo-acoustic coupling is a likely
399 mechanism. Those stations that do not show increased amplitudes near the power line are located
400 almost exclusively at the southern-most power line in our study area (Fig. 2d), indicating that this
401 power line has potentially been inactive during the deployment.

402 Gas Pipelines

403 Several gas pipelines cross the study region, transferring gas to and from one of Europe's largest
404 gas hubs, the Baumgarten gas hub (Fig. 2d). While the gas hub itself is a clear source of seismic
405 energy (Fig. 2b, c), our findings on the gas pipelines themselves are less conclusive. Note that for
406 the stations near the gas hub, only very little data is available (Fig. 1).

407 We do not find clearly increased amplitudes near gas pipelines (Fig. 2). PSDs that are
408 corrected for cross-contamination (Fig. S2g), however, suggest that we do in fact observe slightly
409 increased amplitudes at around 3 Hz to 11 Hz, compared to no known nearby sources (Fig. S2h).
410 There is a slight separation of amplitudes that shows roughly two maxima at this frequency range.

411 We find that the stations with higher amplitudes are located towards the west of the study area, near
412 Gänserndorf. In the maps of amplitude levels, we have probably overlooked this effect due to many
413 nearby sources (Fig. 2). This further suggests that the increased amplitude levels between 3 Hz and
414 11 Hz are indeed not related to the gas pipelines, but to other strong sources more than 400m away.
415 In fact, we do not find a clear distance-dependency at 10Hz, or any other frequency (Fig. 4).

416 In principle, the flow of gas through pipelines should generate at least some pipe-motion.
417 However, friction between the gas and the pipe walls is expected to be very low, for laminar flow. If
418 one could record gas pipeline activity with seismometers, monitoring of pipeline health becomes an
419 attractive prospect. For high resolution, distributed acoustic sensing could be utilized to get low-cost
420 and high-resolution measurements of the pipes' state in real time (Zhan, 2019). At this point, the
421 signal level seems to be quite low though.

422 Airplanes

423 The array recorded airplanes travelling to and from the Vienna International Airport, the 14th
424 largest airport in Europe. The airport is located ~ 25km to the south-southwest of the center of the
425 study area. Airplanes generate unique high-frequency signals with clear and distinct Doppler effect
426 (Fig. 5i). Meng & Ben-Zion (2018) described the spectral features of air traffic as recorded on
427 seismograms in great detail and our measurements have striking resemblance to their observations
428 and modelling of moving airplanes. We do observe a first overtone for all airplanes (e.g., Fig. 5i), a
429 feature that Meng & Ben-Zion (2018) did not observe for all events. Air traffic signals have to couple
430 seismo-acoustically into the ground and seismometers, there is no other reasonable mechanism. The
431 fact we record these signals so clearly indicates the potential of this mechanism for seismoacoustic
432 research. The acoustic waves that have been generated primarily have been converted into seismic
433 waves, which we observe. Acoustic-seismic coupling as observed here is currently a topic of

434 research, and these observations can very well help to further understand this phenomenon (e.g.,
435 Schneider et al., 2018; Fuchs et al., 2019).

436 **Impact on Green's Function retrieval**

437 The above mentioned sources may have significant impact on the retrieval of empirical Green's
438 functions from cross-correlations of the ambient seismic field. In particular, windmills act as
439 stationary seismic sources that emit energy continuously, a property they share with ocean-generated
440 noise. Such stationary seismic sources inside of the array likely introduce additional strong arrivals
441 in cross-correlation functions (CCFs), as the assumption of a scattered wave-field or uniform source
442 distribution is clearly violated. Still, these CCFs could be sensitive to the subsurface structure, and
443 may certainly be useful for monitoring applications at frequencies above the microseismic frequency
444 band. When aiming at extracting estimated Green's functions from CCFs for imaging purposes,
445 however, these additional arrivals may dominate the signal and identifying the phase related to direct
446 inter-station wave-propagation may prove challenging. Roux et al. (2016) used double-beamforming
447 to filter the extracted wavefield in CCFs to only allow for certain wavenumbers, and thus propagation
448 directions. They used this approach to extract surface waves from a body-wave-dominated wave field.
449 Such an approach should allow to filter out waves propagating from the location of the windmills, at
450 least for some station pairs, potentially enabling subsurface-imaging based on inter-station surface
451 wave velocities even in the presence of strong continuous sources.

452 **Conclusions**

453 We demonstrate that dense seismic arrays allow unique and detailed insight into the spatio-temporal
454 properties of the ambient seismic field at frequencies above the microseisms. Our results complement

455 previous work by other authors on other arrays and some of the sources we observe. We investigate
456 seismic data of an array of 10,532 stations deployed in the eastern Vienna basin for one week.
457 Sources of seismic energy that we observe and describe include windmills of different types, a
458 railway track, trains, oil pumpjacks, cars, power lines, and air traffic. All sources exhibit distinctly
459 different spectral and temporal features that allow to describe them, and possible to identify them
460 (automatically).

461 We find that at frequencies most relevant to imaging of shallow subsurface structure with
462 ambient-noise-based surface waves (up to \sim 10 Hz), windmills, the railway track, and oil pumpjacks
463 emerge as the primary sources of seismic energy in the study area. Windmills in particular act
464 as stationary sources that continuously emit strong seismic energy and may introduce unwanted
465 secondary wave fields in ambient noise cross-correlation functions. Oil pumpjacks exhibit similar
466 properties, but are less dominant in the seismic records. Because of the high station density, we can
467 fit the amplitude decay with distance at different frequencies, and give indications for the propagation
468 regimes of different source-induced wave fields and thus their coupling mechanisms. Windmills,
469 potentially couple by directly shaking the ground at frequencies around 1 Hz, while coupling
470 seismo-acoustically at higher frequencies, indicated by spherical amplitude decay. Similarly, power
471 lines also appear to couple seismo-acoustically at the power grid frequency and below due to corona
472 discharge.

473 This study is intended to motivate further studies on this data set, which may include
474 ambient-noise-based surface-wave tomography, extraction of body waves from the ambient seismic
475 field, and signal detection and identification, as well as seismoacoustics.

476 **Data and Resources**

477 Seismograms used in this study were collected using an array for industrial exploration by OMV
478 E&P GmbH. They can be made available upon request to OMV E&P GmbH. The supplemental
479 material includes animated videos of amplitude levels over time, as well as some observations on
480 non-anthropogenic sources. Meteorological data from the station Zwerndorf has been provided
481 by Manfred Dorninger. The software used in this study was kindly provided by Beyreuther et al.
482 (2010) and Virtanen et al. (2020). The colormap used for illustrations in this study was provided by
483 Crameri (2018).

484 **Acknowledgements**

485 The authors thank OMV E&P GmbH for access to the seismic data, and the permission to publish
486 these results. Part of this work was performed using funding from the Austrian Science Fund
487 (FWF): Projects 26391 and 30707. The authors are grateful to Florian Fuchs, Petr Kolínský, Andrew
488 Delorey, Artemii Novoselov, Manfred Dorninger, and Dimitri Zigone for insightful comments and
489 discussions.

490 **List of Figure Captions**

- 491 • Figure 1: Map of the study area at the Austria-Slovakia border, just northeast of Vienna (see
492 insert). The array consists of 10,532 stations with 40m inline- and 400m crossline-spacing.
493 Data is available for up to 92.5 hours and was recorded from January 18th to 23rd 2018
494 (during daytime only).

- 495 • Figure 2: Mean noise amplitudes in three frequency bands (a-c) and potential noise sources
496 in the study area (d). a) At 0.5-2Hz, relatively even distribution of amplitudes with slightly
497 increased amplitude levels in the north, close to the wind farm Prottes-Ollersdorf (PO). b) At
498 2-8Hz, increased amplitudes along a number of low-frequency noise sources: railway track,
499 wind farm PO, oil pumps, and the Baumgarten gas hub. c) At 8-20Hz, roads and power lines
500 emerge as visible noise sources, and increased amplitudes are spatially focused. d) Map of
501 potential noise sources in the study region. Locations of sources extracted and compiled from
502 OpenStreetMap contributors (2017), Interessengemeinschaft Windkraft Österreich (2020),
503 Gas Connect Austria GmbH (2020), and OMV AG (pers. comm.).

- 504 • Figure 3: Binned and stacked power-spectral densities (PSDs) for stations close to the noise
505 sources mapped in Figure 2d, normalized by the total number of stations. The sources are:
506 windmills of wind farm PO (a), other windmills (b), the railway track (c), oil pumps (d), roads
507 (e), power lines (f), gas pipelines (g). Nearby stations are defined as within 200m distance to
508 a given noise source. Stations labelled 'none' (h) are in at least 1000m distance to any noise
509 source. The map view (i) shows the spatial distribution of stations selected for the respective
510 noise sources by color.

- 511 • Figure 4: PSD amplitudes versus distance for the known noise sources at 0.48 Hz, 1.13 Hz,
512 10 Hz, and 50Hz. At 0.48 Hz, no source exhibits a clear decay with distance. At 1.13 Hz, the
513 windmills of PO appear as the only significant noise source that exhibit a distance-dependent
514 decay of amplitude. At 10 Hz, pronounced amplitude-decay for windmills of PO, the railway
515 track, oil pumps, and roads. At 50 Hz, sharp decline in amplitude over short distances for
516 stations near the the railway track, roads, and power lines. Note that at 50 Hz data is shown up
517 to 250m distance, instead of 1000m. Data was fit with power laws (solid lines). The grey lines

518 mark the amplitude decay when excluding stations that do not show increased amplitudes
519 near power lines at 50 Hz.

- 520 • Figure 5: Representative spectrograms (2s windows, 95% overlap) from 10-minute seismo-
521 grams, for different sources: a windmill of PO (a), a different windmill (b), trains (c), a
522 continuously operating oil pump (d), cars (e), a power line (f), a gas pipeline (g), no nearby
523 source (h), and a passing airplane (i). Some sources continuously excite ground motion
524 (a,b,d,f,g), while others are distinct events (c,e,i). The dashed white boxes mark the zoomed-in
525 views in Figure 6.
- 526 • Figure 6: Zoomed-in spectrograms from Figure 5 for a passing train (a), and an oil pump
527 (b). The spectrogram of the passing train exhibits equidistant spectral lines induced by the
528 passing train, as well as a Doppler shift of ~3 Hz. The complex and periodically repeating
529 spectrogram of the oil pump (b) is clearly related to the pumping motion with a period of
530 ~16s.

531 References

- 532 Ardhuin, F., Stutzmann, E., Schimmel, M., & Mangeney, A., 2011. Ocean wave sources of seismic
533 noise, *Journal of Geophysical Research*, **116**(C9), C09004–21.
- 534 Beyreuther, M., Barsch, R., Krischer, L., Megies, T., Behr, Y., & Wassermann, J., 2010. Obspy: A
535 python toolbox for seismology, *Seismological Research Letters*, **81**(3), 530.
- 536 Brenguier, F., Campillo, M., Hadzioannou, C., Shapiro, N. M., Nadeau, R. M., & Larose, E., 2008.
537 Postseismic Relaxation Along the San Andreas Fault at Parkfield from Continuous Seismological
538 Observations, *Science*, **321**(5895), 1478–1481.
- 539 Brenguier, F., Campillo, M., Takeda, T., Aoki, Y., Shapiro, N. M., Briand, X., Emoto, K., & Miyake,
540 H., 2014. Mapping pressurized volcanic fluids from induced crustal seismic velocity drops,
541 *Science*, **345**(6192), 80–82.
- 542 Brenguier, F., Boue, P., Ben-Zion, Y., Vernon, F., Johnson, C. W., Mordret, A., Coutant, O., Share,
543 P. E., Beaucé, E., Hollis, D., & Lecocq, T., 2019. Train Traffic as a Powerful Noise Source for
544 Monitoring Active Faults With Seismic Interferometry, *Geophysical Research Letters*, **46**(16),
545 9529–9536.
- 546 Brenguier, F., Courbis, R., Mordret, A., Campman, X., Boue, P., Chmiel, M., Takano, T., Lecocq,
547 T., Van der Veen, W., Postif, S., & Hollis, D., 2020. Noise-based ballistic wave passive seismic
548 monitoring. Part 1: body waves, *Geophysical Journal International*, **221**(1), 683–691.
- 549 Brix, F. & Schultz, O., 1993. *Erdöl und Erdgas in Österreich*, Naturhistorisches Museum Wien and
550 F. Berger, Horn, Wien.

- 551 Chamarczuk, M., Nishitsuji, Y., Malinowski, M., & Draganov, D., 2019. Unsupervised Learning
552 Used in Automatic Detection and Classification of Ambient-Noise Recordings from a Large-N
553 Array, *Seismological Research Letters*, **91**(1), 370–389.
- 554 Crameri, F., 2018. Geodynamic diagnostics, scientific visualisation and StagLab 3.0, *Geoscientific
555 Model Development*, **11**(6), 2541–2562.
- 556 de Ridder, S. A. L. & Biondi, B. L., 2015. Ambient seismic noise tomography at Ekofisk,
557 *GEOPHYSICS*, **80**(6), B167–B176.
- 558 Dean, T., 2019. The seismic signature of rain, *ASEG Extended Abstracts*, **2018**(1), 1–8.
- 559 Edwards, W. N., 2015. Analysis of Measured Wind Turbine Seismic Noise Generated from the
560 Summerside Wind Farm, Prince Edward Island, Tech. Rep. 7763, Geological Survey of Canada.
- 561 Evers, L. G., Ceranna, L., Haak, H. W., Le Pichon, A., & Whitaker, R. W., 2007. A Seismoacoustic
562 Analysis of the Gas-Pipeline Explosion near Ghislenghien in Belgium, *Bulletin of the Seismological
563 Society of America*, **97**(2), 417–425.
- 564 Fuchs, F., Bokelmann, G., & the AlpArray Working Group, 2017. Equidistant Spectral Lines in
565 Train Vibrations, *Seismological Research Letters*, **89**(1), 56–66.
- 566 Fuchs, F., Schneider, F. M., Kolínský, P., Serafin, S., & Bokelmann, G., 2019. Rich observations
567 of local and regional infrasound phases made by the AlpArray seismic network after refinery
568 explosion, *Scientific Reports*, **9**(13027).
- 569 Garden, M. & Züldsdorff, L., 2019. Acquisition of a modern seismic survey in the Vienna Basin,
570 in *SEG Technical Program Expanded Abstracts 2019*, pp. 253–257, Society of Exploration
571 Geophysicists.

- 572 Gas Connect Austria GmbH, 2020. Location of gas pipelines extracted from <https://www.gasconnect.at/netzinformationen/unser-netz-im-detail/>, last accessed on
573 03.03.2020.
- 575 Gortsas, T. V., Triantafyllidis, T., Chrisopoulos, S., & Polyzos, D., 2017. Numerical modelling of
576 micro-seismic and infrasound noise radiated by a wind turbine, *Soil Dynamics and Earthquake*
577 *Engineering*, **99**, 108–123.
- 578 Hasselmann, K., 1963. A Statistical Analysis of the Generation of Microseisms, *Reviews of*
579 *Geophysics and Space Physics*, **1**, 177–210.
- 580 Hetényi, G., Molinari, I., Clinton, J., Bokelmann, G., Bondár, I., Crawford, W. C., Dessa, J.-X.,
581 Doubre, C., Friederich, W., Fuchs, F., Giardini, D., Gráczer, Z., Handy, M. R., Herak, M., Jia, Y.,
582 Kissling, E., Kopp, H., Korn, M., Margheriti, L., Meier, T., Mucciarelli, M., Paul, A., Pesaresi,
583 D., Piromallo, C., Plenefisch, T., Plomerová, J., Ritter, J., Rümpker, G., Šipka, V., Spallarossa,
584 D., Thomas, C., Tilmann, F., Wassermann, J., Weber, M., Wéber, Z., Wesztergom, V., Živčić,
585 M., Abreu, R., Allegretti, I., Apoloner, M.-T., Aubert, C., Besançon, S., de Berc, M. B., Brunel,
586 D., Capello, M., Čarman, M., Cavaliere, A., Chèze, J., Chiarabba, C., Cougoulat, G., Cristiano,
587 L., Czifra, T., D'Alema, E., Danesi, S., Daniel, R., Dannowski, A., Dasović, I., Deschamps,
588 A., Egdorf, S., Fiket, T., Fischer, K., Funke, S., Govoni, A., Gröschl, G., Heimers, S., Heit, B.,
589 Herak, D., Huber, J., Jarić, D., Jedlička, P., Jund, H., Klingen, S., Klotz, B., Kolínský, P., Kotek,
590 J., Kühne, L., Kuk, K., Lange, D., Loos, J., Lovati, S., Malengros, D., Maron, C., Martin, X.,
591 Massa, M., Mazzarini, F., Métral, L., Moretti, M., Munzarová, H., Nardi, A., Pahor, J., Péquegnat,
592 C., Petersen, F., Piccinini, D., Pondrelli, S., Prevolnik, S., Racine, R., Régnier, M., Reiss, M.,
593 Salimbeni, S., Santulin, M., Scherer, W., Schippkus, S., Schulte-Kortnack, D., Solarino, S.,
594 Spieker, K., Stipčević, J., Strollo, A., Süle, B., Szanyi, G., Szűcs, E., Thorwart, M., Ueding, S.,

- 595 Vallocchia, M., Vecsey, L., Voigt, R., Weidle, C., Weyland, G., Wiemer, S., Wolf, F., Wolyniec,
596 D., & Zieke, T., 2018. The AlpArray Seismic Network: A Large-Scale European Experiment to
597 Image the Alpine Orogen, *Surveys in Geophysics*, **39**(5), 1–25.
- 598 Hu, W., Barthelmie, R. J., Letson, F., & Pryor, S. C., 2019. Seismic Noise Induced by Wind Turbine
599 Operation and Wind Gusts, *Seismological Research Letters*, **91**(1), 427–437.
- 600 Interessengemeinschaft Windkraft Österreich, 2020. A map of windmills can be accessed at
601 [https://www.igwindkraft.at/?xmlval_ID_KEY\[0\]=1055/](https://www.igwindkraft.at/?xmlval_ID_KEY[0]=1055/), last accessed on 03.03.2020.
- 602 Juretzek, C. & Hadzioannou, C., 2016. Where do ocean microseisms come from? A study of
603 Love-to-Rayleigh wave ratios, *Journal of Geophysical Research: Solid Earth*, **121**(9), 6741–6756.
- 604 Juretzek, C. & Hadzioannou, C., 2017. Linking source region and ocean wave parameters with the
605 observed primary microseismic noise, *Geophysical Journal International*, **211**(3), 1640–1654.
- 606 Karplus, M. & Schmandt, B., 2018. Preface to the Focus Section on Geophone Array Seismology,
607 *Seismological Research Letters*, **89**(5), 1597–1600.
- 608 Kästle, E. D., El-Sharkawy, A., Boschi, L., Meier, T., Rosenberg, C., Bellahsen, N., Cristiano,
609 L., & Weidle, C., 2018. Surface Wave Tomography of the Alps Using Ambient-Noise and
610 Earthquake Phase Velocity Measurements, *Journal of Geophysical Research: Solid Earth*, **123**(2),
611 1770–1792.
- 612 Kong, Q., Trugman, D. T., Ross, Z. E., Bianco, M. J., Meade, B. J., & Gerstoft, P., 2018. Machine
613 Learning in Seismology: Turning Data into Insights, *Seismological Research Letters*, **90**(1), 3–14.
- 614 Lecocq, T., Longuevergne, L., Pedersen, H. A., Brenguier, F., & Stammler, K., 2017. Monitoring

- 615 ground water storage at mesoscale using seismic noise: 30 years of continuous observation and
616 thermo-elastic and hydrological modeling, *Scientific Reports*, **7**(1), 1–16.
- 617 Lin, F. C., Moschetti, M. P., & Ritzwoller, M. H., 2008. Surface wave tomography of the western
618 United States from ambient seismic noise: Rayleigh and Love wave phase velocity maps,
619 *Geophysical Journal International*, **173**(1), 281–298.
- 620 Loeb, L. B., 1965. *Electrical Coronas, Their Basic Physical Mechanisms*, University of California
621 Press.
- 622 Longuet-Higgins, M. S., 1950. A theory of the origin of microseisms, *Philosophical Transactions
623 of the Royal Society of London A Mathematical, Physical and Engineering Sciences*, **243**(857),
624 1–35.
- 625 Lu, Y., Stehly, L., Paul, A., & AlpArray Working Group, 2018. High-resolution surface wave
626 tomography of the European crust and uppermost mantle from ambient seismic noise, *Geophysical
627 Journal International*, **214**(2), 1136–1150.
- 628 Meng, H. & Ben-Zion, Y., 2018. Characteristics of Airplanes and Helicopters Recorded by a Dense
629 Seismic Array Near Anza California, *Journal of Geophysical Research: Solid Earth*, **123**(6),
630 4783–4797.
- 631 Mordret, A., Landès, M., Shapiro, N. M., Singh, S. C., Roux, P., & Barkved, O. I., 2013. Near-surface
632 study at the Valhall oil field from ambient noise surface wave tomography, *Geophysical Journal
633 International*, **193**(3), 1627–1643.
- 634 Mordret, A., Roux, P., Boué, P., & Ben-Zion, Y., 2018. Shallow 3-D structure of the San Jacinto
635 Fault zone revealed from ambient noise imaging with a dense seismic array, *Geophysical Journal
636 International*, **216**(2), 1–21.

- 637 Mordret, A., Courbis, R., Brenguier, F., Chmiel, M., Garambois, S., Mao, S., Boué, P., Campman,
638 X., Lecocq, T., Van der Veen, W., & Hollis, D., 2020. Noise-based ballistic wave passive seismic
639 monitoring – Part 2: surface waves, *Geophysical Journal International*, **221**(1), 692–705.
- 640 Nakata, N., Chang, J. P., Lawrence, J. F., & Boué, P., 2015. Body wave extraction and tomography
641 at Long Beach, California, with ambient-noise interferometry, *Journal of Geophysical Research: Solid Earth*, **120**(2), 1159–1173.
- 643 eds Nakata, N., Gualtieri, L., & Fichtner, A., 2019. *Seismic Ambient Noise*, Cambridge University
644 Press, 1st edn.
- 645 OpenStreetMap contributors, 2017. Planet dump retrieved from <https://planet.osm.org> , <https://www.openstreetmap.org>.
- 646
- 647 Ren, Y., Grecu, B., Stuart, G., Houseman, G., Hegedüs, E., & South Carpathian Project Working
648 Group, 2013. Crustal structure of the Carpathian-Pannonian region from ambient noise
649 tomography, *Geophysical Journal International*, **195**(2), 1351–1369.
- 650 Riahi, N. & Gerstoft, P., 2015. The seismic traffic footprint: Tracking trains, aircraft, and cars
651 seismically, *Geophysical Research Letters*, **42**(8), 2674–2681.
- 652 Roux, P., 2009. Passive seismic imaging with directive ambient noise: application to surface waves
653 and the San Andreas Fault in Parkfield, CA, *Geophysical Journal International*, **179**(1), 367–373.
- 654 Roux, P., Moreau, L., Lecointre, A., Hillers, G., Campillo, M., Ben-Zion, Y., Zigone, D., & Vernon,
655 F., 2016. A methodological approach towards high-resolution surface wave imaging of the San
656 Jacinto Fault Zone using ambient-noise recordings at a spatially dense array, *Geophysical Journal
657 International*, **206**(2), 980–992.

- 658 Schippkus, S., Zigone, D., Bokelmann, G., & the AlpArray Working Group, 2018. Ambient-noise
659 tomography of the wider Vienna Basin region, *Geophysical Journal International*, **215**(1),
660 102–117.
- 661 Schneider, F. M., Fuchs, F., Kolínský, P., Caffagni, E., Serafin, S., Dorninger, M., Bokelmann, G., &
662 Group, A. W., 2018. Seismo-acoustic signals of the Baumgarten (Austria) gas explosion detected
663 by the AlpArray seismic network, *Earth and Planetary Science Letters*, **502**, 104–114.
- 664 Spica, Z. J., Nakata, N., Liu, X., Campman, X., Tang, Z., & Beroza, G. C., 2018. The Ambient
665 Seismic Field at Groningen Gas Field: An Overview from the Surface to Reservoir Depth,
666 *Seismological Research Letters*, **89**(4), 1450–1466.
- 667 Stammler, K. & Ceranna, L., 2016. Influence of Wind Turbines on Seismic Records of the Gräfenberg
668 Array, *Seismological Research Letters*, **87**(5), 1075–1081.
- 669 Virtanen, P., Gommers, R., Oliphant, T. E., Haberland, M., Reddy, T., Cournapeau, D., Burovski, E.,
670 Peterson, P., Weckesser, W., Bright, J., van der Walt, S. x. f. J., Brett, M., Wilson, J., Millman,
671 K. J., Mayorov, N., Nelson, A. R. J., Jones, E., Kern, R., Larson, E., Carey, C. J., Polat, a. x. l.,
672 Feng, Y., Moore, E. W., VanderPlas, J., Laxalde, D., Perktold, J., Cimrman, R., Henriksen, I.,
673 Quintero, E. A., Harris, C. R., Archibald, A. M., Ribeiro, A. x. n. H., Pedregosa, F., Mulbregt, P.,
674 Vijaykumar, A., Pietro Bardelli, A., Rothberg, A., Hilboll, A., Kloekner, A., Scopatz, A., Lee,
675 A., Rokem, A., Woods, C. N., Fulton, C., Masson, C., m, C. H. x. g. x., Fitzgerald, C., Nicholson,
676 D. A., Hagen, D. R., Pasechnik, D. V., Olivetti, E., Martin, E., Wieser, E., Silva, F., Lenders,
677 F., Wilhelm, F., Young, G., Price, G. A., Ingold, G.-L., Allen, G. E., Lee, G. R., Audren, H. x.,
678 Probst, I., Dietrich, J. x. r. P., Silterra, J., Webber, J. T., x0010D, J. S., Nothman, J., Buchner, J.,
679 Kulick, J., nberger, J. L. S. x., de Miranda Cardoso, J. x. V. x. c., Reimer, J., Harrington, J., guez,
680 J. L. C. R. x., Nunez-Iglesias, J., Kuczynski, J., Tritz, K., Thoma, M., Newville, M., mmerer, M.

- 681 K. x., Bolingbroke, M., Tartre, M., Pak, M., Smith, N. J., Nowaczyk, N., Shebanov, N., Pavlyk,
682 O., Brodtkorb, P. A., Lee, P., McGibbon, R. T., Feldbauer, R., Lewis, S., Tygier, S., Sievert, S.,
683 Vigna, S., Peterson, S., More, S., Pudlik, T., Oshima, T., Pingel, T. J., Robitaille, T. P., Spura, T.,
684 Jones, T. R., Cera, T., Leslie, T., Zito, T., Krauss, T., Upadhyay, U., Halchenko, Y. O., & zquez
685 Baeza, Y. V. x., 2020. SciPy 1.0: fundamental algorithms for scientific computing in Python,
686 *Nature Methods*, **13**(Suppl. 1), 1–15.
- 687 Zhan, Z., 2019. Distributed Acoustic Sensing Turns Fiber-Optic Cables into Sensitive Seismic
688 Antennas, *Seismological Research Letters*, **91**(1), 1–15.

689 **Authors**690 **Sven SCHIPPKUS**

691 University of Vienna

692 Department of Meteorology and Geophysics,

693 Althanstraße 14,

694 1090 Vienna, Austria

695 sven.schippkus@univie.ac.at

696

697 **Mikaël GARDEN**

698 OMV E&P GmbH,

699 Geophysics Department,

700 Trabrennstraße 6-8,

701 1020 Vienna, Austria

702 mikael.garden@omv.com

703

704 **Götz BOKELMANN**

705 University of Vienna

706 Department of Meteorology and Geophysics,

707 Althanstraße 14,

708 1090 Vienna, Austria

709 goetz.bokelmann@univie.ac.at

710

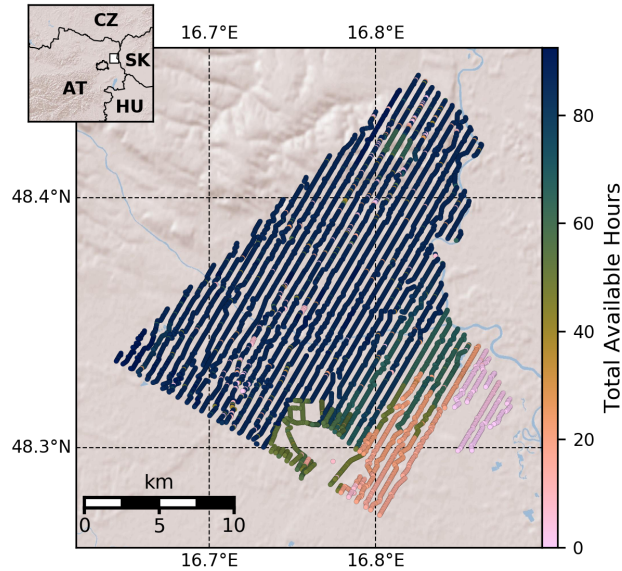
711 **Figures**

Figure 1: Map of the study area at the Austria-Slovakia border, just northeast of Vienna (see insert). The array consists of 10,532 stations with 40m inline- and 400m crossline-spacing. Data is available for up to 92.5 hours and was recorded from January 18th to 23rd 2018 (during daytime only).

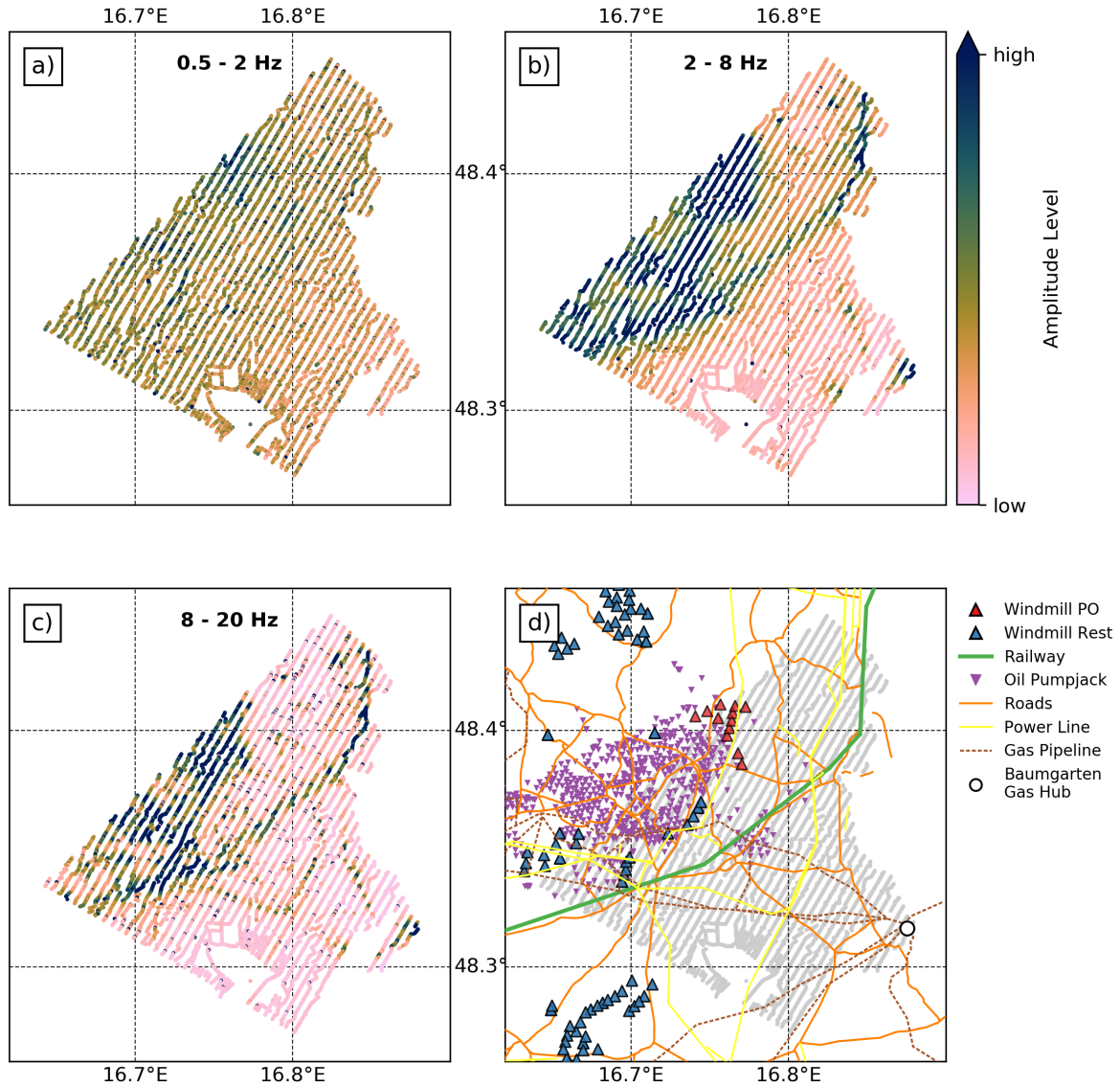


Figure 2: Mean noise amplitudes in three frequency bands (a-c) and potential noise sources in the study area (d). a) At 0.5-2Hz, relatively even distribution of amplitudes with slightly increased amplitude levels in the north, close to the wind farm Prottes-Ollersdorf (PO). b) At 2-8Hz, increased amplitudes along a number of low-frequency noise sources: railway track, wind farm PO, oil pumps, and the Baumgarten gas hub. c) At 8-20Hz, roads and power lines emerge as visible noise sources, and increased amplitudes are spatially focused. d) Map of potential noise sources in the study region. Locations of sources extracted and compiled from OpenStreetMap contributors (2017), Interessengemeinschaft Windkraft Österreich (2020), Gas Connect Austria GmbH (2020), and OMV AG (pers. comm.).

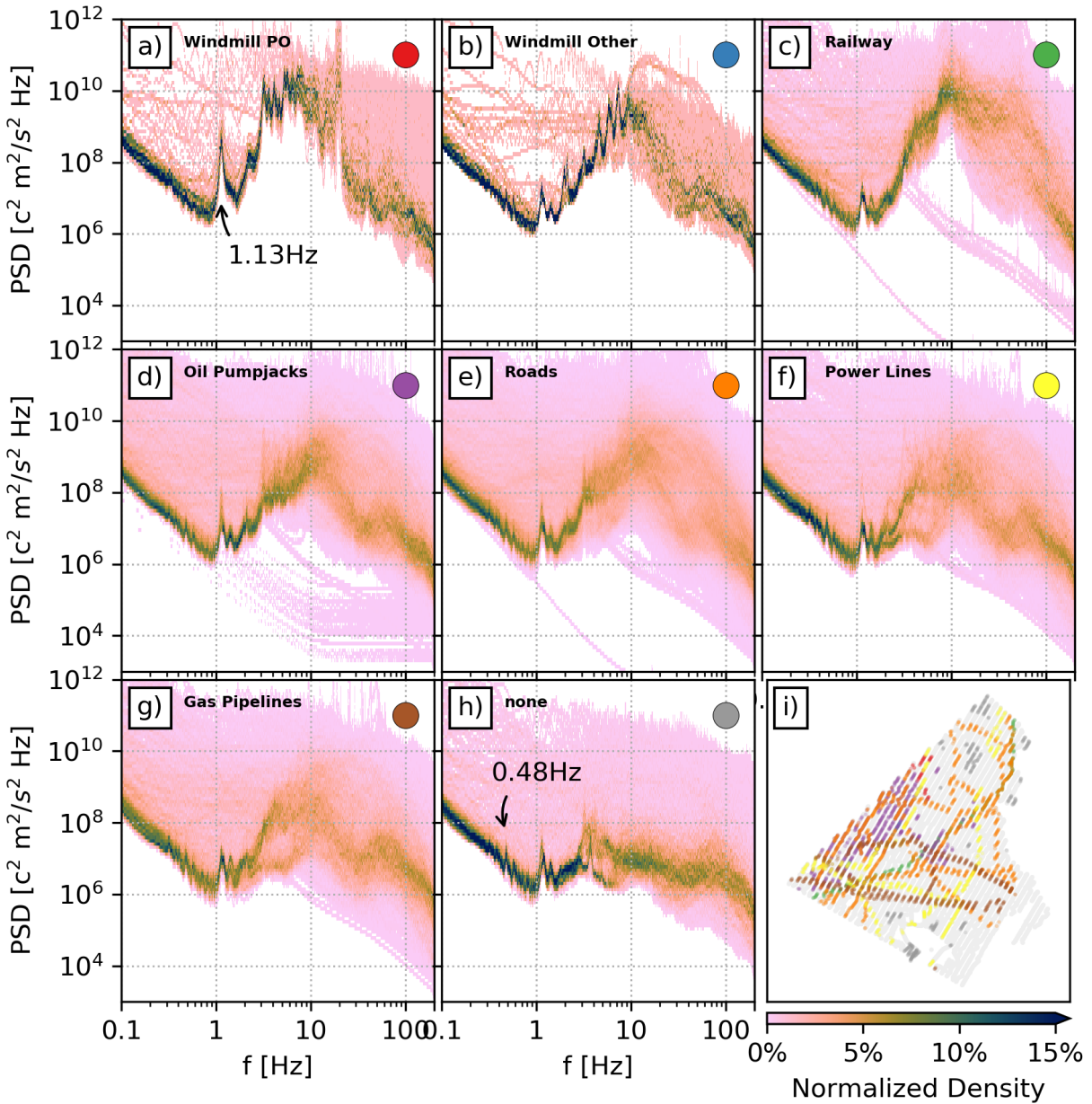


Figure 3: Binned and stacked power-spectral densities (PSDs) for stations close to the noise sources mapped in Figure 2d, normalized by the total number of stations. The sources are: windmills of wind farm PO (a), other windmills (b), the railway track (c), oil pumps (d), roads (e), power lines (f), gas pipelines (g). Nearby stations are defined as within 200m distance to a given noise source. Stations labelled 'none' (h) are in at least 1000m distance to any noise source. The map view (i) shows the spatial distribution of stations selected for the respective noise sources by color.

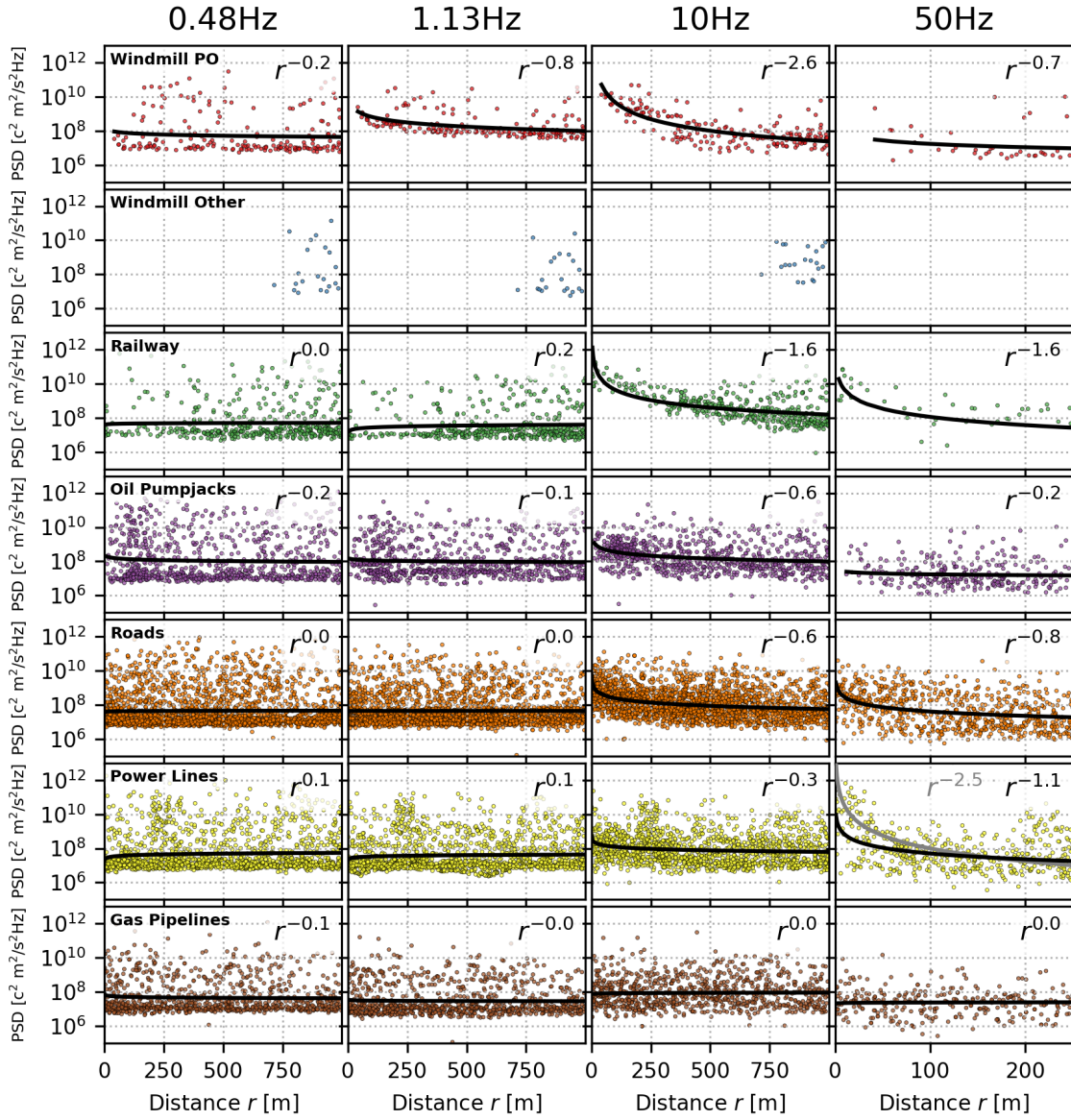


Figure 4: PSD amplitudes versus distance for the known noise sources at 0.48 Hz, 1.13 Hz, 10 Hz, and 50Hz. At 0.48 Hz, no source exhibits a clear decay with distance. At 1.13 Hz, the windmills of PO appear as the only significant noise source that exhibit a distance-dependent decay of amplitude. At 10 Hz, pronounced amplitude-decay for windmills of PO, the railway track, oil pumps, and roads. At 50 Hz, sharp decline in amplitude over short distances for stations near the the railway track, roads, and power lines. Note that at 50 Hz data is shown up to 250m distance, instead of 1000m.
37 Data was fit with power laws (solid lines). The grey lines mark the amplitude decay when excluding stations that do not show increased amplitudes near power lines at 50 Hz.

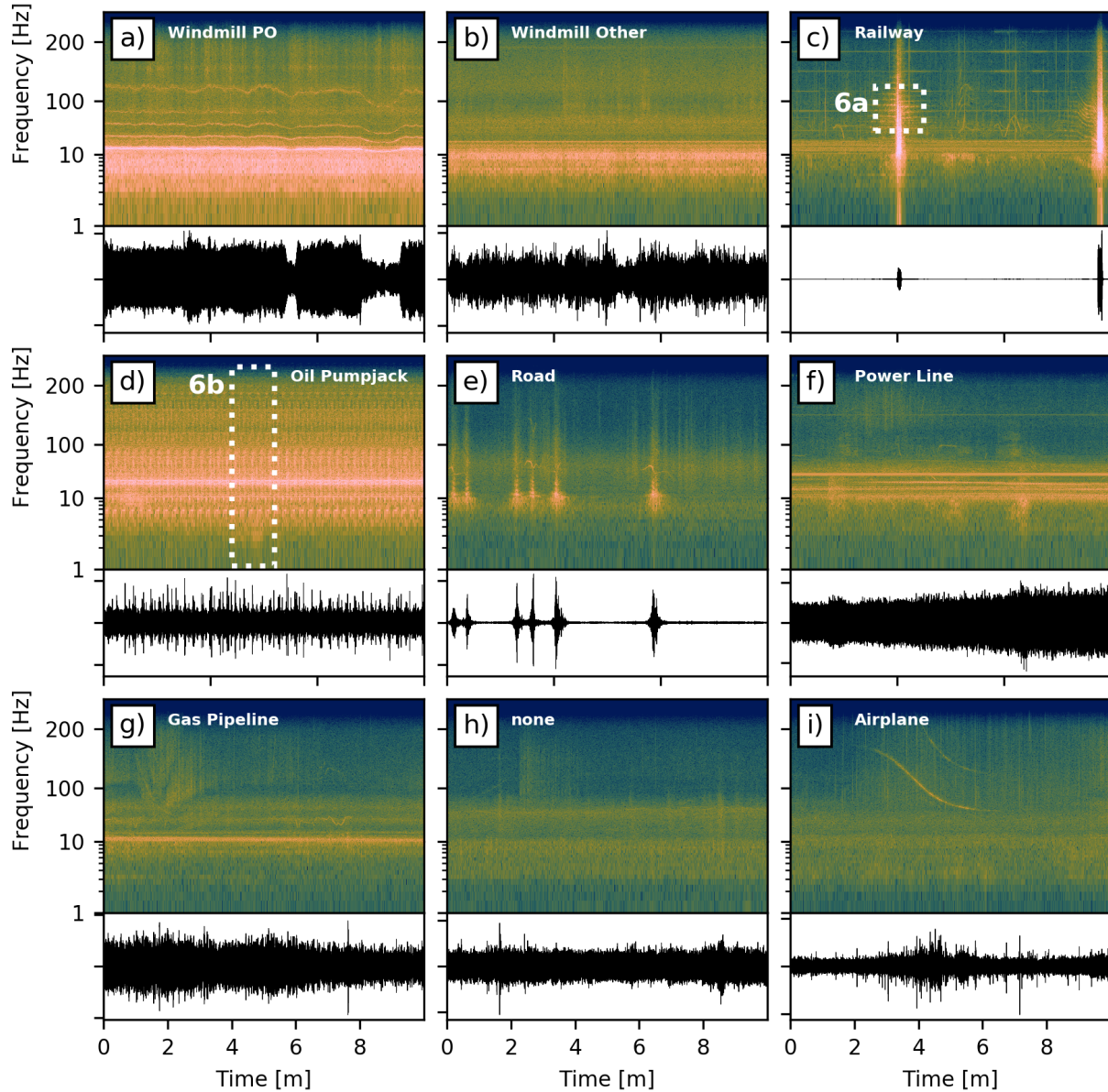


Figure 5: Representative spectrograms (2s windows, 95% overlap) from 10-minute seismograms, for different sources: a windmill of PO (a), a different windmill (b), trains (c), a continuously operating oil pump (d), cars (e), a power line (f), a gas pipeline (g), no nearby source (h), and a passing airplane (i). Some sources continuously excite ground motion (a,b,d,f,g), while others are distinct events (c,e,i). The dashed white boxes mark the zoomed-in views in Figure 6.

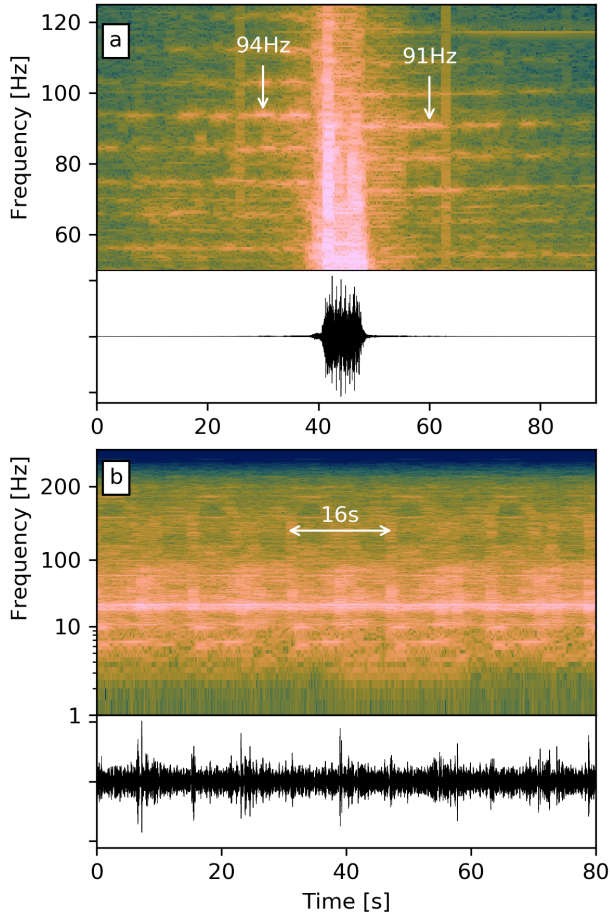


Figure 6: Zoomed-in spectrograms from Figure 5 for a passing train (a), and an oil pump (b). The spectrogram of the passing train exhibits equidistant spectral lines induced by the passing train, as well as a Doppler shift of ~ 3 Hz. The complex and periodically repeating spectrogram of the oil pump (b) is clearly related to the pumping motion with a period of ~ 16 s.

712 **Supplementary Material**

713 **S1 Videos of amplitudes**

714 We provide videos of mean absolute amplitudes, averaged over 1-minute windows, of unfiltered
715 data (Video S1) and data filtered in three frequency bands (Video S2: 0.5-2 Hz, Video S3: 2-8 Hz,
716 Video S4: 8-20 Hz). The videos are provided in the electronic supplement. The top panel in each
717 shows wind speed (orange) and precipitation (blue) data of the meteorological station "Zwerndorf"
718 inside the array (inverted black triangle in the map). Grey sections mark nighttime (22:00 to 06:40
719 UTC), where stations did not record data. These sections are skipped in the videos.

720 The videos enable unique insight into the distribution of seismic energy in space and time.
721 They expose activity of the wind farm Prottes-Ollersdorf, trains moving along the railway track,
722 cars on roads, people walking, and many other sources. The most relevant observations related to
723 anthropogenic sources are described in the main text.

724 In addition to the trends described in the main text, we also observe weather-related events.
725 The most striking one is a passing weather front on January 19th, with locally increased amplitudes
726 at 0.5-2Hz (Video S2). We observe a slowly-moving (a few meters per second) front of increased
727 amplitudes incoming from northwest. Comparison with meteorological data reveals this to coincide
728 with heavy precipitation and increased wind speeds (Fig. S3, Video S2). A different rain event can
729 be seen in the 0.5-2Hz video (Video S2) on January 20th around 6:50 UTC+1, where small patches
730 of emerging amplitudes correspond to rain fall. The precipitation event on January 20th around
731 15:30 UTC+1 that is recorded in meteorological data, however, does not appear to coincide with
732 increased amplitudes on nearby seismic stations. Dean (2019) found that that rain noise is dominant
733 at frequencies above 80Hz. We find rain to be a relevant signal in a very wide frequency band (Fig.

734 S3), and to be most impactful at 0.5-2Hz (Video S2), at least relative to other sources. At higher
735 frequencies, other sources such as oil pumpjacks, trains, cars and even power lines induce much
736 higher amplitudes (Videos S1, S3, S4).

737 **S2 Beamforming and ocean-generated noise**

738 Beam powers are computed for small sub-arrays of six stations each (typical aperture \sim 1 km),
739 distributed evenly inside the array (Fig. S1). The mean beamforming result of those sub-arrays
740 (Fig. S1, top left) shows seismic energy arriving from northwest (301 degrees) to southeast with
741 velocities compatible with Rayleigh waves (3.4 km/s) in a sedimentary-basin setting.

742 This is consistent with ocean-generated noise in the North-Atlantic and commonly observed
743 in central Europe (e.g. Ardhuin et al., 2011; Juretzek & Hadzioannou, 2016, 2017) and also for the
744 Vienna basin in particular (Schippkus et al., 2018). Therefore, this array may be utilized for more
745 "classical" applications of the ambient seismic field that rely on microseismic frequencies, including
746 imaging of the top few kilometers of the crust.

747 This observation illustrates the capability of this array of 10Hz-geophones to resolve such
748 low frequencies, and the potential for applications that utilize the microseismic noise. The strength
749 of the microseismic noise and the fact that 12 or 24 geophones are densely co-located (mitigating
750 self-noise) are likely factors for this capability.

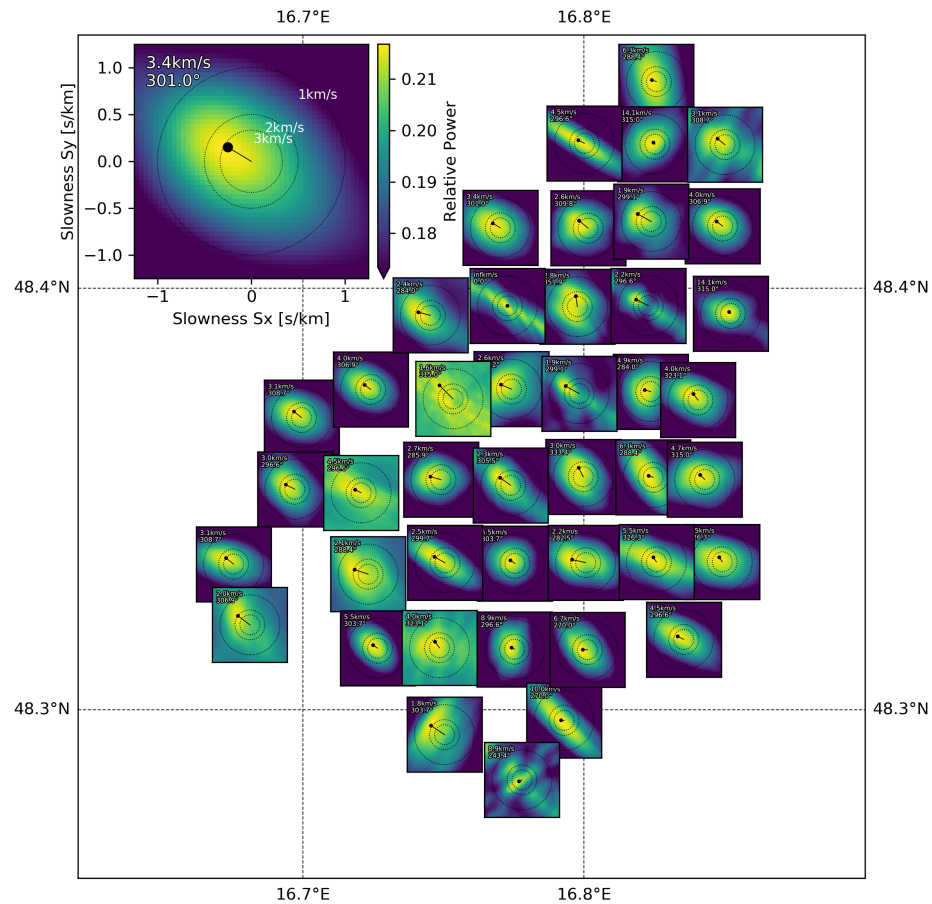


Figure S1: Beamforming results for 0.2-0.5Hz at small sub-arrays (of 6 stations each) distributed throughout the array, and the mean result (top left). The sub-arrays of 10Hz-geophones are capable of resolving frequencies near the secondary microseismic peak ($\sim 0.15\text{Hz}$) and consistently show energy arriving from northwest (301°) to southeast with reasonable Rayleigh-wave velocities (3.4km/s).

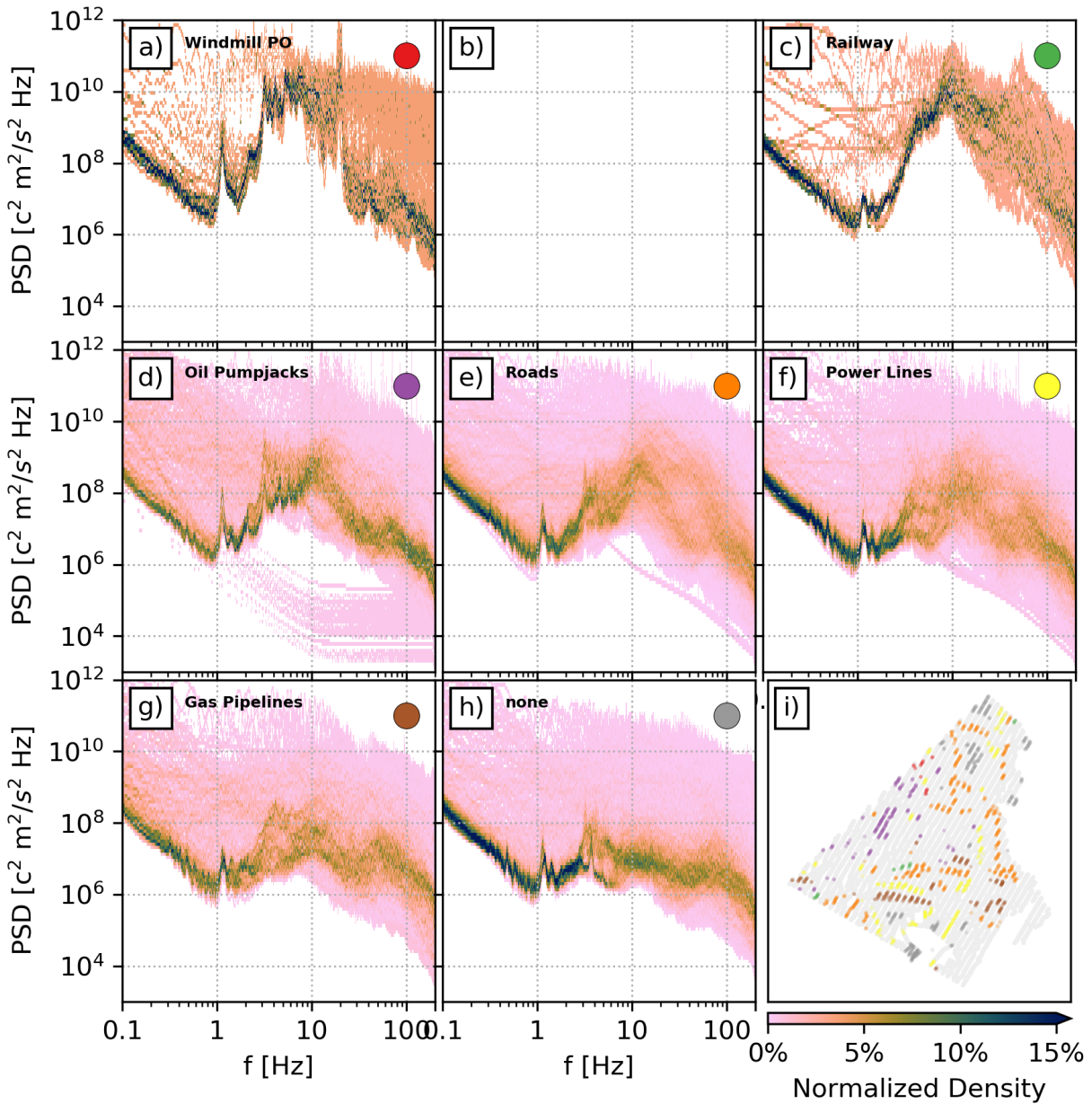


Figure S2: Same as Figure 3, but used stations are limited to those that are within 200m distance to the given noise source and at least 400m away from any other noise source to avoid cross-contamination. This selection further focuses individual contributions of some sources, e.g., oil pumps and the railway track. Windmills not part of the wind farm PO are removed entirely, because these windmills are located in the west of the study area, near other sources (Fig. 2d).

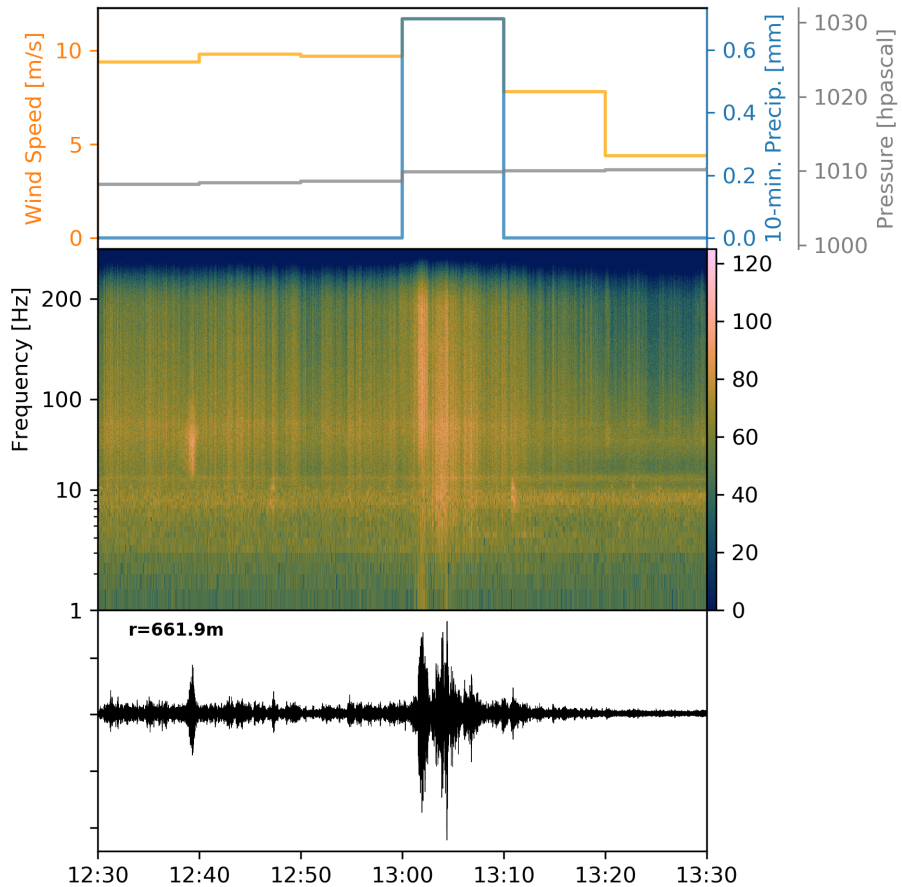


Figure S3: Weather event on January 19th 2018. In the 0.5-2Hz amplitude video (Video S2), a band of increased amplitude levels can be seen propagating from northwest with velocities of a few meters per second. Meteorological data of a station inside the array (top panel) reveals this to be a passing rain front with heavy precipitation, increased wind speeds, and a jump in atmospheric pressure. The meteorological data has 10-minute sampling rate. The lower panels show the spectrogram and seismic trace of a station in 662m distance from the meteorological station.